Developmental changes in hippocampal neurite colocalize with the expression of genes involved in modulating low-theta oscillations

*Kember, J.[1], Gracia-Tabuenca, Z.[1,2], Patel, R. [3,4], Chakravarty, M.[4], Chai, X.J.[1]

1. Montreal Neurological Institute & Hospital, McGill University, Montréal, QC H3A 2B4.
2. Department of Statistics, University of Zaragoza, C. de Pedro Cerbuna, 12, 50009 Zaragoza, Spain.
3. Cerebral Imaging Centre, Douglas Mental Health University Institute, Verdun, Québec, H4H 1R3, Canada.
4. Department of Biomedical Engineering, McGill University, 845 Rue Sherbrooke O, Montréal, QC H3A 0G4.

Author email addresses: jonah.kember@mail.mcgill.ca (*corresponding author), zeus@unizar.es, mohammed.patel@psych.ox.ac.uk, mallar.chakravarty@mcgill.ca, xiaoqian.chai@mail.mcgill.ca

Keywords: Hippocampus, MRI microstructure, development, adolescence, neurite orientation dispersion and density imaging (NODDI), low-theta oscillations, memory encoding.

Abstract

The hippocampus is a critical brain structure that supports the encoding and retrieval of episodic memories, yet the intricate development of its microstructure in humans remains unknown. Understanding this microstructural maturation and how it relates with the maturation of hippocampal function may provide critical insight into the basic mechanisms underlying memory and their disruption in disease. To address this gap, we non-invasively estimated the density and branching complexity of neurite (dendrites, axons, glial processes) using diffusion-weighted MRI in 364 participants aged 8–21. We found that these microstructural measures differ between subfields and along the longitudinal axis of the hippocampus. Notably, we observed spatially heterogeneous increases in the branching complexity of neurite until approximately 15 years of age, with prominence in CA1, stratum radiatum/lacunosum/moleculare, subiculum, and the anterior hippocampus. Furthermore, our imaging transcriptomics analysis shed light on the molecular underpinnings of these developmental dynamics. Regions exhibiting substantial age-related increases in neurite orientation dispersion also tend to express genes associated with the modulation of low-theta oscillations during memory encoding. These results suggest that the protracted maturation of hippocampal microstructure may be linked to the development of low-theta oscillation modulations during encoding.

Introduction

In the cortex, thin extensions from the neural soma– axons, dendrites, glial processes– collectively known as neurite, play a fundamental role in shaping regional circuits and in the emergence of functional processes. Neurite properties vary across brain structures, and within the same structure, for instance, along the transverse and longitudinal axes of the adult hippocampus (Beaujoin et al., 2018; Karat et al., 2023). Some evidence suggests a relationship between neurite microstructure and electrophysiological signal properties, such as the generation and modulation of oscillatory neurophysiological activity related to synaptic potentiation and memory (Andrade-Talavera et al., 2023; Kota et al., 2020; Malik et al., 2016; Tukker et al., 2013).

During child and adolescent development, the density and branching complexity of neurites increase across association cortices (Lynch et al., 2023; Zhao et al., 2021). However, it is currently unclear whether similar microstructural development unfolds in the hippocampus. Moreover, it is presently unknown how such microstructural development relates to the electrophysiological activity of hippocampal circuits relevant to memory. Understanding this link may be crucial in explaining the basic mechanisms underlying memory and their disruption in various neurodevelopmental disorders (Li et al., 2019; Ofen et al., 2019).

The primary dimension of microstructural organization in the hippocampus is across its subfields: distinct regions topographically localized across the medial-lateral axis which include CA1–CA4, dentate gyrus, and the subiculum (Andersen et al., 2007). The second most prominent dimension of microstructural organization is along the anterior to posterior longitudinal axis of the hippocampus (Masouleh et al., 2020). The defining microstructural properties of each subfield are typically identified from post-mortem histological tissue samples. However, recent work with diffusion-weighted magnetic resonance imaging (MRI)

suggests that hippocampal substructures can be delineated non-invasively and *in vivo* (Beaujoin et al., 2018; Karat et al., 2023; Zhang et al., 2012).

Across the cortex, MRI-derived measures of tissue microstructure are correlated with the magnitude of frequency band-specific oscillations in extracellular field potentials source-localized via magnetoencephalography (Baillet, 2017; Shafiei et al., 2023). In the hippocampus, electrophysiological signal properties vary across subfields and along the longitudinal axis, reflecting at least in part changes in tissue microstructure. For instance, low-theta (2-5 Hz) oscillations are the most prominent pattern of electrophysiological activity recorded in the hippocampus and are the strongest in CA1 and the stratum radiatum/lacunosum/moleculare (SRLM). The phase of low-theta oscillations modulates the magnitude of gamma oscillations (>40Hz) and the firing of action potentials differentially in CA1, CA3, and Dentate Gyrus (Buzsaki et al., 2002; Mizuseki et al., 2009). Along the longitudinal axis, the magnitude of low-theta oscillations at rest and during memory encoding increase from posterior to anterior hippocampus (Goyal et al., 2020; Lin et al., 2017). Because of these regional differences in electrophysiological signaling, an understanding of how microstructural development unfolds differently across subfields and longitudinal-positions may help link microstructural development with developmental changes in electrophysiology.

In the current study, we sought to identify age-related differences in the properties of neurites within the hippocampus between childhood and young adulthood, and to investigate how these microstructural changes might relate to development of the electrophysiological mechanisms underlying memory encoding. To do so, we examined how diffusion-MRI markers of neurite density and branching complexity differed across subfields and along the longitudinal axis in 364 participants between 8 and 21 years of age from the Lifespan Human Connectome Project Development (HCP-D) data, using both Neurite Orientation Dispersion

and Density Imaging (NODDI) and Diffusion Tensor Imaging (DTI) measures. Next, we investigated how these microstructural properties covaried with differences in age throughout late childhood and adolescence using a multivariate technique capturing the variance in age that is shared with a measure of hippocampal-dependent episodic memory function. We then make use of a data-driven imaging transcriptomics approach, where we spatially integrate our neuroimaging data with transcriptomic data from the Allen human brain gene-expression atlas (Arnatkevic□iūtė et al., 2019; Hawrylycz et al., 2012; Paus et al., 2023) to investigate whether there is co-localization of the genes related to memory-encoding mechanisms and hippocampal microstructure development. Such a colocalization would inform how the structural maturation of the hippocampus is related with the maturation of the electrophysiological mechanisms underlying memory encoding. In these analyses, we focus on six previously identified gene sets, each related with a specific 'oscillatory subsequent memory effect' (SME). Oscillatory SMEs are differences in the magnitude (v^2/Hz) of narrowband frequencies within the electrocorticogram signal between the presentation of stimuli which are later remembered and equivalent stimuli which are later forgotten (Berto et al., 2018; Berto et al., 2021).

Results

Distinct microstructural profiles in subfields and longitudinal-positions

To quantify microstructure, we examined the neurite density index (NDI) and orientation dispersion index (ODI) derived from NODDI, as well as metrics derived from DTI (mean diffusivity, MD; axial diffusivity, AD; radial diffusivity, RD; Zhang et al., 2012; Alexander et al., 2007). We extracted these 5 microstructural metrics (NDI, ODI, MD, AD, RD) in 5 hippocampal subfields (CA1, SRLM, DG/CA4, CA3/CA2, subiculum; average across right/left hippocampus) from each subject's diffusion MRI imaging data (see Methods for subfield segmentation). For longitudinal-position analyses, we divided each subject's

hippocampus mask into three parts of equal length along the longitudinal axis. We then derived the average of each microstructural metric across each of these three segments: the anterior (hippocampus head), middle (body), and posterior third (tail), similar to published approaches (Solar et al., 2021; DeMaster et al., 2014; Lee et al., 2020).

We first quantified the degree to which the subfield and anterior-posterior ROIs showed unique microstructural profiles, on average, across subjects. We performed a Partial Least Squares-Discriminant analysis (PLS-DA) to test for latent variables (PLS components) which account for the respective variance in tissue microstructure while significantly discriminating between ROIs (McIntosh et al., 2004; Brereton & Lloyd, 2014). This analysis provides interpretable components based on microstructural properties that distinguish subfields from one another, and tests whether these components can classify ROIs significantly above chance-level. We conducted separate PLS-DA analyses for subfields and longitudinal-positions.

The PLS-DA analysis of subfield microstructure identified 3 PLS components that accounted for 58.4%, 22.5%, and 18.3% of the microstructural variance, respectively, and were able to classify subfields at significantly ($p < .05$) above chance level (Figure 1A). The mean cross-validated accuracies for support vector classifiers trained on these components were: PLS1: .37 [.34, .40], PLS2: .40 [.37, .43], PLS3: .29 [.24, .34] (Figure 1B; chance-level: .20; [95% CI] reported). The microstructural metrics that significantly loaded onto these components were MD and RD onto PLS1, and NDI onto PLS2. No microstructural measures significantly loaded onto PLS3 (Figure 1C). Scatterplots and kernel density plots showing PLS, PLS2, and PLS3 scores for each subfield, which indicate the distribution of PLS-component scores for each subfield, are presented in Figure 1D. As can be seen from the loadings of the PLS components and the kernel density plots, subfield microstructures primarily differ in terms of mean diffusivity, radial diffusivity, and neurite density estimates;

with a pronounced difference in MD/RD in the subiculum, and NDI in CA3/CA2. For NDI, these results are generally consistent with findings in adults: values are relatively high in CA3/CA2 and low in CA1 (Karat et al., 2023).

The PLS-DA analysis along the longitudinal axis of the hippocampus identified a single PLS component, which accounted for 40.0% of the variance in our microstructural data, and could classify longitudinal-position at significantly above chance-level. The accuracy for a classifier trained on this component was .65 [.58, .72] (chance-level: . *3*; [95% CI] reported), with only ODI significantly loading onto this component (Figure 2C). Kernel density plots of PLS1 scores for each longitudinal-position are shown in Figure 2D. These data indicate that the orientation dispersion of neurites is the microstructural property that varies the most along the longitudinal axis of the hippocampus; with relatively high orientation dispersion in the anterior/body hippocampus, and low orientation dispersion (i.e., greater orientation cohesion) in the posterior hippocampus. This finding is similar to work in adults, where ODI is higher in the anterior relative to the posterior hippocampus (Karat et al., 2023).

Hippocampal microstructure relates to age and memory differences (multivariate analysis)

We then tested how individual differences in microstructure across subfields covary with differences in age and memory performance in this developmental sample, using multivariate PLS analysis (Figure 3). We assessed memory performance via the NIH Toolbox Picture Sequence Memory Test scores. The PLS analysis identified a single latent variable that accounted for 20.6% of the variance in subfield microstructure, and 27.8% of the variance in age and memory. No other PLS components were significant (as can be seen by the steep drop off in the variance in the age/memory matrix accounted for by subsequent PLS components: see the scree plot in Figure 3C). Both age and memory significantly and

positively loaded onto PLS1. Thirteen microstructural features significantly loaded onto PLS1, showing that increases in age/memory are associated with: increased NDI in all subfields, increased ODI in three subfields (CA1, SRLM, subiculum), decreased RD in DG/CA4, increased RD and MD in subiculum, decreased AD in subiculum, and increased AD in CA3/CA2. The loadings of each subject onto the microstructure matrix (*X*) and age/memory matrix (*Y*) can be seen in Figure 3D. These results reveal a significant but heterogeneous relationship between subfield microstructures, age, and memory.

We repeated the same approach to assess whether individual differences in microstructure along the longitudinal axis covary with individual differences in age and memory (Figure 4). We found a latent variable that significantly accounted for 24.7% of the variance in our microstructure measures along the longitudinal axis of the hippocampus, and 26.1% of the variance in age and memory. The loadings of this component suggest that increases in NDI and ODI across the longitudinal axis of the hippocampus, and lower AD values in the head of the hippocampus are associated with increases in age and memory performance. Interestingly, the microstructural metrics that discriminate subregions along the anterior–posterior axis are different from those that discriminate subfields: ODI discriminated between anterior and posterior hippocampus, but not subfields. This indicates that the longitudinal gradient in neurite branching complexity is not subfield-dependent, rather, it is present across subfields.

Diffusion-MRI measures of neurite are predictive of age and memory

The multivariate analyses above suggested that measures of NDI and ODI might be most sensitive to individual differences in age and memory performance. We therefore tested the degree to which each microstructural metric (for all ROIs) could independently predict age and memory through ordinary least-squares regression. Specifically, we tested whether a linear model with the mean of each microstructural metric for all ROIs as features could

predict either age or memory above chance-level (= .05). For instance, to quantify the degree to which NDI predicts age, we fit the model: Age = $\beta_0 + \beta_1$NDI-CA1 + β_2NDI-CA4/DG + β_3NDI-CA3/CA2 + β_4NDI-SRLM + β_5NDI-Subiculum.

We found that individual differences in each microstructural metric were significantly predictive of age. However, NDI and ODI accounted for significantly more variance in age than MD, AD, and RD (Figure 5: see 95% confidence intervals for measures of significance). For memory performance (the residuals, after controlling for age), no regression models were significant. Taken together, these results suggest that NDI and ODI are particularly sensitive to individual differences in age.

Age related differences in NDI and ODI across development

To more precisely characterize how NDI and ODI change with age across development within each subfield and along the longitudinal axis of the hippocampus, we predicted NDI and ODI as functions of age in each subregion using non-linear models (NDI shown in Figure 6; ODI shown in Figure 7). We observed large age-related differences in NDI across all subfields, with out-of-sample R^2 values (estimated through 5-fold cross-validation) ranging from .28 to .37. The extent to which age was predictive of NDI did not significantly differ between any subfield (one-way ANOVA p = .45), suggesting age-related differences in NDI are relatively homogenous across the hippocampus. In contrast, the extent to which age was was predictive of ODI was dependent on the subregions (one-way ANOVA $p < 1.0 \times 10^{-9}$). Age was predictive of ODI in CA1 (.44 ± .02), SRLM (.21 ± .04), and subiculum (.34 ± .03), but not in DG/CA4 (-.003 ± .02) or CA3/CA2 (-.002 ± .01; mean out-of-sample R^2, ± standard error of the mean across cross-validation folds). Similar findings were observed along the longitudinal axis of the hippocampus. The extent to which age was predictive of NDI (out-of-sample R^2) was not significantly dependent on longitudinal position (one-way ANOVA p = .18), while the extent to which age was predictive of ODI was

significantly dependent on longitudinal position ($p = 5.1 \times 10^{-3}$). Specifically, age was significantly more predictive of ODI in the anterior hippocampus ($R^2 = .34 \pm .017$) than both the body ($R^2 = .20 \pm .028$) and the posterior hippocampus ($R^2 = .16 \pm .040$).

Taken together, these results suggest that individual differences in both the density and branching complexity of neurites in the hippocampus are correlated with age. However, while correlations between neurite density (NDI) and age are observed indiscriminately across the entire hippocampus, correlations between branching complexity (ODI) and age are localized to specific regions: CA1, SRLM, subiculum, and the anterior hippocampus. Qualitatively, ODI followed a general pattern characterized by an increase from 8 until roughly 15 years of age, followed by little to no age-related change from 15 to 21 years of age.

Expression of genes involved in modulating low-theta oscillations colocalize with age-related differences in the branching complexity of neurite

Our results so far show age-related differences in both NDI and ODI across the hippocampus, with ODI differences varying by subfield and along the longitudinal axis. To understand the functional implications these differences may have, we investigated whether age-related differences in NDI or ODI spatially aligned with the expression of oscillatory SME gene sets identified by Berto et al. (2021) using PLS. The expression of genes within these sets has been shown to correlate with the degree to which oscillations in the electrocorticogram differ between subsequently remembered and forgotten visual stimuli (Berto et al., 2021). To quantify the relationship between NDI and ODI with age at each gene expression site, we simply predicted age from the mean NDI and ODI at that location (averaged across the voxel of the gene-expression site, plus its immediately adjacent voxels, totalling 27 mm^3) through ordinary least squares regression (Age ~ NDI + ODI) and took the coefficients from this model (NDI- , ODI-). We then tested whether these values

covaried, across gene-expression sites, with the expression of the SME-gene sets using PLS. In the PLS analysis comparing age-related change in ODI and the WM12 gene-set, for instance, *Y* is the age-related change in ODI at each hippocampal-site, and *X* is the expression of WM12 genes at each hippocampal site (a [Site x Gene] matrix).

We found for the gene-set WM12 a significant latent variable that accounted for 26.3% of variance in the region-by-gene expression matrix and 16.0% of variance in ODI-□ (Figure 8; FWE-$p < .05$, corrected for 6 gene-sets and two microstructure measures)). This effect was specific to WM12: age-related differences in ODI did not significantly colocalize with the other tested gene-sets (WM11: $p = .21$, WM19: $p = .16$, WM21: $p = .24$, WM22: $p = .25$; minimum *p*-value across the row-permutation and gene-set permutation tests). Next, we ran a gene ontology analysis of the 79 genes within WM12 which positively loaded onto this latent PLS component. We found that these genes were significantly associated with 14 cellular components, and 9 molecular functions (FDR-$p < .05$; Figure 8). The cellular components and molecular functions at the top of the PANTHER classification system hierarchy were: postsynaptic membrane, postsynaptic density, cation channel complex, somatodendritic compartment, neuron projection, and high voltage-gated calcium channel activity (Figure 8D and 8E).

We then examined the spatial distribution of scores on the WM12-PLS component across the two hippocampal axes. These scores represent a linear combination of the genes in WM12, with weights shown in Figure 8A. We observed positive scores on the WM12-PLS component for gene expression sites within SRLM and the anterior hippocampus, and negative scores for DG/CA4 and the posterior hippocampus (one-sample *t*-test, *p*'s < .05; Figure 9). Together, these results suggest that regions with large age-related differences in neurite branching complexity, namely SRLM and anterior hippocampus, also tend to show

relatively higher expression of genes in the WM12 gene-set– genes which are associated with the modulation of low-theta oscillations during memory encoding.

Discussion

Using a biophysical model of diffusion-weighted MRI sensitive to the density and branching complexity of neurite, we offer the first glance at how these properties come to vary along the prominent axes of hippocampal organization throughout childhood and adolescence. While we observed age-related differences in the density of neurite across the entire hippocampus, differences in the branching complexity of neurite were primarily confined to CA1/SRLM, the subiculum, and the anterior portion of the hippocampus. Interestingly, these age-related differences spatially colocalized with the expression of genes that are involved in modulating low-theta oscillations during memory encoding. This colocalization suggests that developmental changes in the branching complexity of neurite may be linked with differences in the way low-theta oscillations are modulated during encoding. These results contribute to our understanding of the basic mechanisms underlying memory development.

We found that the set of genes which colocalize with age-related differences in neurite branching complexity are significantly expressed in the somatodendritic compartment and in voltage-gated ion channels. Previous work suggests these gene sets regulate low-theta oscillations during memory encoding (Berto et al., 2018; Berto et al., 202). Previous cell-type enrichment analyses have found these genes to be overrepresented in deep-layer pyramidal neurons, as well as SST^+, VIP^+, and PV^+ inhibitory interneurons (Berto et al., 2021). Together, these results (i.e, that the genes involved in regulating low-theta are expressed in voltage-gated ion channels in the somatodendritic compartment of pyramidal and inhibitory interneurons) suggest this gene set may regulate low-theta oscillations through the modification of conductances at excitatory-inhibitory synapses.

The specific mechanisms driving developmental changes in hippocampal microstructure throughout the peripubertal period are poorly understood. However, the age-related differences in ODI we observed (increases throughout late childhood and peaks at around 15 years old) are reminiscent of association cortex during this time window. For instance, changes in the structure (e.g., cortical thickness) and function (e.g., low-frequency fluctuations in the blood-oxygenation level dependent signal) of transmodal cortex follow a similar pattern (Raznahan et al., 2011; Tamnes et al., 2018; Sydnor et al., 2023; Sydnor et al., 2021). In the aforementioned instances, peripubertal increases are often brought on by increased inhibitory signaling from PV^+ interneurons, and reflect the opening of 'sensitive periods' where synaptic plasticity is maximal (Larsen et al., 2022; Sydnor et al., 2021). Similar mechanisms may help explain adolescent changes in hippocampal microstructure as well. Indeed, evidence in rodent models suggests this may be the case. Specifically, in the CA1 subfield of mice, puberty is associated with an increase in the dendritic branching of PV^+ interneurons, as well as an increase in the expression of the GABA receptor δ-subunit; changes which disinhibit the PV^+ interneurons, and greatly increase the strength of inhibitory currents to CA1 pyramidal neurons (Shen et al., 2020).

Our hippocampal microstructure results are supported by several previous findings. First, the increase in neurite density with age across different hippocampal subfields is in line with previous work from Mah et al. (2017), who found NDI across the whole hippocampus to increase with age from 8 to 13 years old. However, Mah et al. (2017) did not observe any age-related differences in ODI, on average, across the hippocampus. In light of current findings, it is likely that averaging across the entire hippocampus obscured the age effects, since ODI age effects varied in different subregions. Second, in line with work from Karat et al. (2023), we found that the branching complexity of neurite is higher in the anterior relative to the posterior hippocampus. Finally, in line with a growing body of literature, we found that

NODDI is significantly more sensitive to the age-related differences observed in gray matter throughout late childhood and adolescence than DTI (Genc et al., 2020). This is likely a result of the enhanced biological specificity provided by the NODDI model, which takes into account the geometry of cells and their projections, and assumes realistic values for intracellular, extracellular, and free-water diffusion. This is in contrast to the DTI model, which assumes all diffusion within a voxel can be captured by a single tensor. Our results are strengthened by the large sample size, high-resolution T1 images (submillimeter), and accurate segmentation protocol (MAGeT; Chakravarty et al., 2013).

These findings demonstrate how age-related differences in tissue microstructure come to vary in the hippocampus along its primary axes of organization throughout childhood and adolescence. The intricate spatial variation of these age-related differences overlapped with a previously identified set of genes linked to the modulation of low-theta oscillations during memory encoding. These findings suggest the protracted maturation of the hippocampus may be associated with an increase in the degree to which low-theta oscillations are evoked during encoding. Ultimately, understanding the pathway linking developmental changes in microstructure with electrophysiological encoding mechanisms may provide key insight into the development of memory and its disruption in disease.

Methods

Participants

Data for the current study were obtained from the development cohort of the Human Connectome Project (HCP-D; Somerville et al., 2018). Subjects in the HCP-D are healthy/typically developing; i.e., they were subjected to extensive exclusion criteria including: prior head injuries, psychiatric illness (Schizophrenia, Bipolar disorder, Anxiety, Major depression), and the reception of special services at school (e.g., for dyslexia, intellectual disabilities, speech/language pathology; see full criteria in Somerville et al.,

2018). All unrelated subjects were initially included in analyses (*N* = 545). Two stringent quality-control procedures were applied (described in greater detail below), resulting in the removal of 136 subjects due to low quality T1 images, and removal of 45 subjects due to low-quality alignment of diffusion-weighted and T1 images (≥ 10 'misaligned' voxels, classified as non-gray matter prior to transformation and within the hippocampus following transformation). This resulted in a total of 364 subjects entering analyses, aged 8.0 to 21.9 years old (*M* = 14.14, *SD* = 3.99), with 193 females and 171 males. Of these subjects, 218 finished the NIH Toolbox Picture Sequence Memory Test for Assessing Clinical Memory Function (Standardized scores: *M* = 110.33, *SD* = 14.18; Weintraub et al., 2013).

MRI data acquisition

Images were acquired with a Siemens 3T Prisma scanner (80 mT/m gradients, slew rate of 200T/m/s) and Siemens 32-channel Prisma head coil (Harms et al., 2018). One T1-weighted image and 21 minutes of diffusion-weighted imaging were acquired (Harms et al., 2018). T1-weighted images had 0.8 mm isotropic voxels (sagittal FOV = 256 x 240 x 166 mm, matrix size = 320 x 300 x 208 slices, slice oversampling of 7.7%, 2-fold in-place acceleration in phase encode direction, bandwidth = 744 Hz/pixel), TR/TI = 2500/1000, TE = 1.8/3.6/5.4/7.2 ms, a flip angle = 8°, and up to 30 TRs. To suppress signals from fat (bone marrow and scalp fat), water excitation was employed. Diffusion weighted images (DWI) had an MB factor of 4, 1.5 mm isotropic voxels, TR = 3.23 s, partial Fourier factor = 6/8, and no in-plane acceleration. 185 diffusion-weighting directions, each with opposite phase encoding (AP and PA) on two shells (b = 1500 s/mm^2, 3000 s/mm^2), were used over four dMRI runs with 28 b = 0 s/mm^2 volumes interspersed (Harms et al., 2018; Somerville et al., 2018).

Hippocampus segmentation

Raw T1-weighted images were preprocessed using the minc-bpipe-library pipeline [https://github.com/CoBrALab/minc-bpipe-library], which includes N4 bias field correction,

registration to MNI space (ICBM 2009a Nonlinear Symmetric), brain extraction using BEaST (Bussy et al., 2021), and standardization through ANTs, minc-toolkit, and MNI priors. The hippocampus was segmented into CA1, subiculum, CA4/dentate gyrus, CA2/CA3, and stratum radiatum/lacunosum/moleculare (SRLM) using the Multiple Automatically Generated Templates (MAGeT) technique (Chakravarty et al., 2013). Segmentations were run separately for left and right hemispheres, and manually controlled for quality by SZ and SG based, resulting in 409 unique subjects (327 with right hemisphere data; 268 with left hemisphere data).

Diffusion-weighted image processing

Raw diffusion weighted images were denoised using Marchenko-Pastur PCA (MRtrix3; Tournier et al., 2019), corrected for eddy current-induced distortions and subject head motion (FSL; Jenkinson et al., 2012), and corrected for distortion due to magnetic field nonlinearity (FreeSurfer; Fischl et al., 2012). Following preprocessing, the diffusion tensor was fitted using all available non-zero *b* values, to facilitate comparison with the metrics derived from NODDI (Broad et al., 2019; Grussu et al., 2015; fitting done with *dwi2tensor*, MRtrix3; Tournier et al., 2019). While less specific than NODDI, these DTI metrics help situate our results within previous work interrogating gray matter microstructure (Nazeri et al., 2020). The NODDI model was fitted with the parameters specified in the *WatsonSHStickTortIsoV_B0* model (those originally described in Zhang et al., 2012) with the exception of intrinsic parallel diffusivity ($d_{\parallel}$), which was fixed at 1.10 $\square m^2/s$. Contemporary evidence suggests this may be the optimal choice when interrogating gray matter (Guerrero et al., 2019; Kraguljac et al., 2022; Genç et al., 2018; Fukutomi et al., 2018; Karat et al., 2023).

Both the diffusion tensor and NODDI were fit in their native space. Transformations registering DTI/NODDI parameter volumes to population space were created and applied using Advanced Normalization Tools (*ants*; Avants et al., 2011). For each subject, all $b = 0$

diffusion-weighted images were averaged, and this mean *b*0 image was rigid-transformed to the T1 image. Then, the T1 image (which had the highest resolution) was non-linearly registered to the population average. This transformation was created separately for right and left hemispheres, and was focused with a 'bounding-box' inclusive of the hippocampus. This bounding box (used for all participants) was created in population space, and included any voxels that fell within the hippocampus of a single subject, plus 5mm along each *x*, *y*, and *z* direction. To ensure accurate transformations, T1 images were segmented into 3-tissues (WM, GM, CSF) using FSL's *fast*, and subjects with transformations that resulted in 10 or more 'misaligned' voxels (i.e, voxels that fell within the hippocampus yet were not classified as gray matter) were removed from further analyses, leaving 279 subjects with right hemisphere data and 230 with left hemisphere data. Segmentations were then manually inspected by JK, although this did not result in the removal of any subjects.

Partial least squares

Partial least squares (PLS) is a general multivariate analysis commonly used on wide data sets with high multicollinearity. Given two *n*-by-*p* matrices *X* and *Y*, PLS identifies linear combinations of the features in *X* and linear combinations of the features in *Y* (latent variables) which have maximum covariance. This approach has several convenient properties. Rather than maximizing the variance in a single matrix (i.e., *X* in PCA; *Y* in multivariate regression), PLS ensures a meaningful amount of variance in both matrices is captured (lowering the risk of overfitting). In addition, since *Y* is defined as a matrix, multiple dependent variables can be included in analyses. In the current context, this means latent variables can capture microstructural variance that is relevant to both age and measures of memory function.

In PLS, the columns of each matrix are *z*-scored, the correlation matrix between *X* and *Y* is computed, and the singular value decomposition of this matrix is taken. The singular

value from this decomposition is proportional to the covariance between *X* and *Y*. The significance of each latent variable was determined through permutation testing, and the significance of each feature's contribution to the latent variable (so-called feature 'salience') was determined through bootstrapping, as described by McIntosh et al. (2004). Specifically, permutation testing involved randomly ordering the rows in *X* 1,000 times, deriving a null distribution of singular values from each permuted-*X*, and testing whether the empirical singular value fell outside the 99th percentile (a Monte-Carlo *p*-value of .01). Bootstrapping involved: (1) randomly re-sampling (with replacement) the rows in both *X* and *Y* 1,000 times, (2) calculating the standard deviation of the coefficients across those samples (the 'bootstrapped standard error'), and (3) taking the ratio between the estimated coefficients and their bootstrapped standard errors. These so-called bootstrapped-ratios are approximately equivalent to *z*-scores (McIntosh et al., 2004), and can therefore be used for significance testing. Analyses were conducted using *plsregress* in the Statistics and Machine Learning toolbox of Matlab R2022b (which implements the SIMPLS algorithm) and in-house scripts (see Code Availability).

PLS-DA

To understand how microstructural properties of the hippocampus varied across subfields and the longitudinal axis, we used a version of PLS modified for categorical *Y* variables (Partial least squares- Discriminant analysis, PLS-DA; Lee et al., 2018). First, subfields were dummy-coded into indicator variables to create the *Y* matrix. Second, the significance of each PLS component was assessed by the ability of a support-vector classifier (with a linear kernel) to classify subfields. When assessing classifier performance, 5-fold cross-validation was used, with the *z*-score normalization, PLS-DA fitting, and support-vector classification implemented completely independently across folds. These analyses were implemented in scikit-learn version 1.3.1 (Pedregosa et al., 2011).

PLS matrices

For analyses examining differences in microstructure across subfields and longitudinal-positions, a ROI-by-microstructure matrix (rows: ROIs, columns: microstructural metrics) were created for each subject, and these were vertically stacked to create *X*; *Y* was a dummy-coded matrix containing ROI labels.

To identify age/memory-related differences in microstructure, a ROI by microstructure matrix (*X*) was created (where each row is a subject and each column is a microstructural-metric/ROI combination), and an age/memory matrix (*Y*) was created (each row is a subject, columns are Age and Memory-scores).

Kernel density estimates

Kernel density estimates are a smooth and continuous alternative to a histogram, both of which simply estimate the density of data-points along a given dimension.. Here, they were used in the text to facilitate the visualization of: (1) the distributions of PLS scores (Figures 1 and 2), and (2) the singular values estimated through permutation testing (Figure 8). These were implemented via the matlab function *ksdensity*.

Curve fitting

To estimate the value of a given microstructural metric as a function of age, we used smoothing splines. These function estimates minimize the mean squared error (MSE), while being penalized by the integral of the second derivative. This penalty is weighted by a hyperparameter (λ), which controls the 'smoothness' of the fit. With no penalty ($\lambda = 0$), the resultant function interpolates the points in *X*; with a sufficiently large penalty ($\lambda >> 0$), the resultant function is linear (Hastie et al., 2009). Here, to avoid overfitting, the smoothing parameter was selected through cross-validation. Specifically, λ was selected to minimize the average MSE across 5-cross validation folds. Splines were estimated using *MATLAB's*

statistics and machine learning toolbox, with cross-validation/plotting implemented through in-house scripts (see code availability).

Imaging transcriptomics

Preprocessing

Data were cross-referenced against post-mortem gene expression data from the Allen Human Brain Atlas (AHBA; Hawrylycz et al., 2012). To increase reproducibility, we obtained a subset of AHBA data that had already been processed for hippocampus-specific analyses by Vogel et al. (2020). Probe values in this preprocessed data are the standardized residuals from a linear model that included dummy-coded donor-ID variables; thus, probe values reflect average gene-expression, independent of inter-individual differences. MNI coordinates in this data are those re-processed by Devenyi (2018) to account for errors that arose from transformations into MNI space (Arnatkevic□iūtė et al., 2019, Vogel et al., 2020).

From this data, genes not expressed in the hippocampus (according to the Human Protein Atlas: [https://www.proteinatlas.org]) were filtered out. Then, since multiple probes index the expression of single genes in the AHBA, we took the mean expression across probes for each gene (Arnatkevic□iūtė et al., 2019). To exclude sites whose voxels did not overlap with our subject's hippocampi, we first created right and left 'majority-vote masks', which included voxels that fell within the hippocampus of half our subjects or more. Then, gene-expression sites whose MNI coordinates fell outside the hippocampal mask were removed. Finally, for a given gene-expression site, the MNI coordinate voxel, and all 26 of its immediately adjacent voxels, were defined as a neighbourhood, resulting in a 27mm^3 box for each gene-expression site. The output of these analyses was a 107 region by 12,180 gene matrix with normalized gene expression levels for all hippocampal sites.

Previous work identifying these gene sets was conducted in the superior/middle temporal gyrus (Brodmann area 38), not the hippocampus. Thus, to ensure the genes within

the coexpression modules did indeed show correlated expression profiles across the hippocampus, we tested whether the variance accounted for by the 'eigengene' of each module (the 1st principal component of the region by gene-set matrix) was significantly greater than the variance accounted for by 1,000 randomly drawn gene sets of equal size. Modules WM11, WM12, WM19, WM21, WM22 were significant (Bonferroni-corrected $p < .05$), while WM4 ($p = .74$) was not.

Imaging derived phenotypes

To quantify the age-related change in NDI and ODI at a given gene-expression site, we predicted age from both metrics using ordinary least squares regression (i.e., Age ~ NDI + ODI; each column *z*-scored). The □'s for each feature were taken as measures of age-related change in those features at a given gene-expression site (a so-called imaging-derived phenotype; IDP). All participants with data available at the site of interest were included. We tested whether either IDP (NDI-□, ODI-□) spatially correlated with the expression of genes within the six gene-sets identified by Berto et al. (2021) using partial least squares. *X* was the region-by-gene expression matrix, and *Y* was the IDP. Gene ontology analyses were performed at [http://geneontology.org/] for Homo Sapiens.

Similar to the PLS analyses conducted with age, we tested for significance using a row-permutation approach. However, this approach does not account for spatial autocorrelation (whereby sites closer to one another will have both similar gene expression values and age-related change in microstructure). Thus, we also tested whether the singular value from the PLS between our IDP and gene-set expression matrix fell outside the 99.17th percentile of a distribution created with 1,000 randomly drawn gene sets of equal size (each consisting of genes expressed in the hippocampus, Bonferroni-corrected for 6 gene-set comparisons; Wei et al., 2022).

References

Alexander, D. C., Dyrby, T. B., Nilsson, M., & Zhang, H. (2019). Imaging brain microstructure with diffusion MRI: practicality and applications. *NMR in Biomedicine*, 32(4), e3841.

Andrade-Talavera, Y., Fisahn, A., & Rodríguez-Moreno, A. (2023). Timing to be precise? An overview of spike timing-dependent plasticity, brain rhythmicity, and glial cells interplay within neuronal circuits. *Molecular Psychiatry*, 1-12.

Arnatkevic□iūtė, A., Fulcher, B. D., & Fornito, A. (2019). A practical guide to linking brain-wide gene expression and neuroimaging data. *Neuroimage*, 189, 353-367.

Baillet, S. (2017). Magnetoencephalography for brain electrophysiology and imaging. *Nature Neuroscience*, 20(3), 327-339.

Bayrak, Ş., de Wael, R. V., Schaare, H. L., Hettwer, M. D., Caldairou, B., Bernasconi, A., ... & Valk, S. L. (2022). Heritability of hippocampal functional and microstructural organization. *NeuroImage*, 264, 119656.

Beaujoin, J., Palomero-Gallagher, N., Boumezbeur, F., Axer, M., Bernard, J., Poupon, F., ... & Poupon, C. (2018). Post-mortem inference of the human hippocampal connectivity and microstructure using ultra-high field diffusion MRI at 11.7 T. *Brain Structure and Function*, 223, 2157-2179.

Berto, S., Wang, G. Z., Germi, J., Lega, B. C., & Konopka, G. (2018). Human genomic signatures of brain oscillations during memory encoding. *Cerebral Cortex*, 28(5), 1733-1748.

Berto, S., Fontenot, M. R., Seger, S., Ayhan, F., Caglayan, E., Kulkarni, A., ... & Konopka, G.

(2021). Gene-expression correlates of the oscillatory signatures supporting human episodic memory encoding. *Nature neuroscience*, 24(4), 554-564.

Buzsáki, G. (2002). Theta oscillations in the hippocampus. *Neuron*, 33(3), 325-340.

Caballero, A., Diah, K. C., & Tseng, K. Y. (2013). Region□specific upregulation of parvalbumin□, but not calretinin□positive cells in the ventral hippocampus during adolescence. *Hippocampus*, 23(12), 1331-1336.

Chakravarty, M. M., Steadman, P., Van Eede, M. C., Calcott, R. D., Gu, V., Shaw, P., ... & Lerch, J. P. (2013). Performing label□fusion□based segmentation using multiple automatically generated templates. *Human brain mapping*, 34(10), 2635-2654.

DeMaster, D., Pathman, T., Lee, J. K., & Ghetti, S. (2014). Structural development of the hippocampus and episodic memory: developmental differences along the anterior/posterior axis. *Cerebral cortex*, 24(11), 3036-3045.

Devenyi, G. A. (2018). gdevenyi/AllenHumanGeneMNI: Nonlinear registration (1.0). Zenodo. https://doi.org/10.5281/zenodo.2483290

Dimsdale-Zucker, H. R., Ritchey, M., Ekstrom, A. D., Yonelinas, A. P., & Ranganath, C. (2018). CA1 and CA3 differentially support spontaneous retrieval of episodic contexts within human hippocampal subfields. *Nature communications*, 9(1), 294.

Goyal, A., Miller, J., Qasim, S. E., Watrous, A. J., Zhang, H., Stein, J. M., ... & Jacobs, J. (2020). Functionally distinct high and low theta oscillations in the human hippocampus. *Nature communications*, 11(1), 2469.

Grussu, F., Schneider, T., Tur, C., Yates, R. L., Tachrount, M., Ianuş, A., ... & Gandini Wheeler□Kingshott, C. A. (2017). Neurite dispersion: a new marker of multiple sclerosis spinal cord pathology? *Annals of clinical and translational neurology*, 4(9), 663-679.

Hawrylycz, M. J., Lein, E. S., Guillozet-Bongaarts, A. L., Shen, E. H., Ng, L., Miller, J. A., ...

& Jones, A. R. (2012). An anatomically comprehensive atlas of the adult human brain transcriptome. *Nature*, 489(7416), 391-399.

Kamiya, K., Hori, M., & Aoki, S. (2020). NODDI in clinical research. *Journal of Neuroscience Methods*, 346, 108908.

Karat, B. G., DeKraker, J., Hussain, U., Köhler, S., & Khan, A. R. (2023). Mapping the macrostructure and microstructure of the in vivo human hippocampus using diffusion MRI. *Human brain mapping*, *44*(16), 5485–5503. https://doi.org/10.1002/hbm.26461

Kota, S., Rugg, M. D., & Lega, B. C. (2020). Hippocampal theta oscillations support successful associative memory formation. *Journal of Neuroscience*, 40(49), 9507-9518.

Kraguljac, N. V., Guerreri, M., Strickland, M. J., & Zhang, H. (2023). Neurite orientation dispersion and density imaging in psychiatric disorders: a systematic literature review and a technical note. *Biological Psychiatry Global Open Science*, 3(1), 10-21.

Lee, J. K., Fandakova, Y., Johnson, E. G., Cohen, N. J., Bunge, S. A., & Ghetti, S. (2020). Changes in anterior and posterior hippocampus differentially predict item-space, item-time, and item-item memory improvement. *Developmental Cognitive Neuroscience*, 41, 100741.

Larsen, B., Cui, Z., Adebimpe, A., Pines, A., Alexander-Bloch, A., Bertolero, M., ... & Satterthwaite, T. D. (2022). A developmental reduction of the excitation: inhibition ratio in association cortex during adolescence. *Science Advances*, 8(5), eabj8750.

Lynch, K. M., Cabeen, R. P., & Toga, A. W. (2023). Spatiotemporal patterns of cortical microstructural maturation in children and adolescents with diffusion MRI. *bioRxiv*, 2023-03.

Mah, A., Geeraert, B., & Lebel, C. (2017). Detailing neuroanatomical development in late childhood and early adolescence using NODDI. *PLoS One*, 12(8), e0182340.

Masouleh, S. K., Plachti, A., Hoffstaedter, F., Eickhoff, S., & Genon, S. (2020). Characterizing the gradients of structural covariance in the human hippocampus. *Neuroimage*, 218, 116972.

Martinez-Heras, E., Grussu, F., Prados, F., Solana, E., & Llufriu, S. (2021, October). Diffusion-weighted imaging: recent advances and applications. *In Seminars in Ultrasound, CT and MRI* (Vol. 42, No. 5, pp. 490-506). WB Saunders.

McIntosh, A. R., & Lobaugh, N. J. (2004). Partial least squares analysis of neuroimaging data: applications and advances. *Neuroimage*, 23, S250-S263.

Mizuseki, K., Sirota, A., Pastalkova, E., & Buzsáki, G. (2009). Theta oscillations provide temporal windows for local circuit computation in the entorhinal-hippocampal loop. *Neuron*, 64(2), 267-280.

Nazeri, A., Schifani, C., Anderson, J. A., Ameis, S. H., & Voineskos, A. N. (2020). In vivo imaging of gray matter microstructure in major psychiatric disorders: opportunities for clinical translation. *Biological Psychiatry: Cognitive Neuroscience and Neuroimaging*, 5(9), 855-864.

Ng, W. P., Cartel, N., Roder, J., Roach, A., & Lozano, A. (1996). Human central nervous system myelin inhibits neurite outgrowth. *Brain research*, 720(1-2), 17-24.

Paus, T. (2022). Tracking development of connectivity in the human brain: axons and dendrites. *Biological Psychiatry*.

Johansen-Berg, H., & Behrens, T. E. (Eds.). (2013). Diffusion MRI: from quantitative measurement to in vivo neuroanatomy. *Academic Press*.

Juraska, J. M., & Drzewiecki, C. M. (2020). Cortical reorganization during adolescence:

What the rat can tell us about the cellular basis. *Developmental Cognitive Neuroscience*, 45, 1

Li, Y., Shen, M., Stockton, M. E., & Zhao, X. (2019). Hippocampal deficits in neurodevelopmental disorders. *Neurobiology of learning and memory*, 165, 106945.

Lin, J. J., Rugg, M. D., Das, S., Stein, J., Rizzuto, D. S., Kahana, M. J., & Lega, B. C. (2017). Theta band power increases in the posterior hippocampus predict successful episodic memory encoding in humans. *Hippocampus*, 27(10), 1040-1053.00857.

Malik, R., Dougherty, K. A., Parikh, K., Byrne, C., & Johnston, D. (2016). Mapping the electrophysiological and morphological properties of CA1 pyramidal neurons along the longitudinal hippocampal axis. *Hippocampus*, 26(3), 341-361.

Okaty, B. W., Miller, M. N., Sugino, K., Hempel, C. M., & Nelson, S. B. (2009). Transcriptional and electrophysiological maturation of neocortical fast-spiking GABAergic interneurons. *Journal of Neuroscience*, 29(21), 7040-7052.

Ofen, N., Tang, L., Yu, Q., & Johnson, E. L. (2019). Memory and the developing brain: From description to explanation with innovation in methods. *Developmental cognitive neuroscience*, 36, 100613.

Park, K., Lee, J., Jang, H. J., Richards, B. A., Kohl, M. M., & Kwag, J. (2020). Optogenetic activation of parvalbumin and somatostatin interneurons selectively restores theta-nested gamma oscillations and oscillation-induced spike timing-dependent long-term potentiation impaired by amyloid β oligomers. *BMC biology*, 18, 1-20.

Raznahan, A., Shaw, P., Lalonde, F., Stockman, M., Wallace, G. L., Greenstein, D., ... & Giedd, J. N. (2011). How does your cortex grow? *Journal of Neuroscience*, 31(19), 7174-7177.

Shafiei, G., Fulcher, B. D., Voytek, B., Satterthwaite, T. D., Baillet, S., & Misic, B. (2023).

Neurophysiological signatures of cortical micro-architecture. *bioRxiv : the preprint server for biology*, 2023.01.23.525101. https://doi.org/10.1101/2023.01.23.525101

Shen, H., Kenney, L., & Smith, S. S. (2020). Increased dendritic branching of and reduced δ-GABAA receptor expression on parvalbumin-positive interneurons increase inhibitory currents and reduce synaptic plasticity at puberty in female mouse CA1 hippocampus. *Frontiers in Cellular Neuroscience*, 14, 203.

Solar, K. G., Treit, S., & Beaulieu, C. (2021). High resolution diffusion tensor imaging of the hippocampus across the healthy lifespan. *Hippocampus*, 31(12), 1271-1284.

Somerville, L. H., Bookheimer, S. Y., Buckner, R. L., Burgess, G. C., Curtiss, S. W., Dapretto, M., ... & Barch, D. M. (2018). The Lifespan Human Connectome Project in Development: A large-scale study of brain connectivity development in 5–21 year olds. *Neuroimage*, 183, 456-468.

Strüber, M., Sauer, J. F., & Bartos, M. (2022). Parvalbumin expressing interneurons control spike-phase coupling of hippocampal cells to theta oscillations. *Scientific Reports*, 12(1), 1362.

Sydnor, V. J., Larsen, B., Bassett, D. S., Alexander-Bloch, A., Fair, D. A., Liston, C., ... & Satterthwaite, T. D. (2021). Neurodevelopment of the association cortices: Patterns, mechanisms, and implications for psychopathology. *Neuron*, 109(18), 2820-2846.

Sydnor, V. J., Larsen, B., Seidlitz, J., Adebimpe, A., Alexander-Bloch, A. F., Bassett, D. S., ...

& Satterthwaite, T. D. (2023). Intrinsic activity development unfolds along a sensorimotor–association cortical axis in youth. *Nature Neuroscience*, 1-12.

Tamnes, C. K., Bos, M. G., van de Kamp, F. C., Peters, S., & Crone, E. A. (2018).

Longitudinal development of hippocampal subregions from childhood to adulthood. *Developmental Cognitive Neuroscience*, 30, 21Vogel, J. W., La Joie, R., Grothe, M. J.,

Tukker, J. J., Lasztóczi, B., Katona, L., Roberts, J. D. B., Pissadaki, E. K., Dalezios, Y., ... & Somogyi, P. (2013). Distinct dendritic arborization and in vivo firing patterns of parvalbumin-expressing basket cells in the hippocampal area CA3. *Journal of neuroscience*, 33(16), 6809-6825.

Vogel, J. W., La Joie, R., Grothe, M. J., Diaz-Papkovich, A., Doyle, A., Vachon-Presseau, E., ... & Evans, A. C. (2020). A molecular gradient along the longitudinal axis of the human hippocampus informs large-scale behavioral systems. *Nature communications*, 11(1), 960.

Vos de Wael, R., Larivière, S., Caldairou, B., Hong, S. J., Margulies, D. S., Jefferies, E., ... & Bernhardt, B. C. (2018). Anatomical and microstructural determinants of hippocampal subfield functional connectome embedding. *Proceedings of the National Academy of Sciences*, 115(40), 10154-10159.

Wei, Y., de Lange, S. C., Pijnenburg, R., Scholtens, L. H., Ardesch, D. J., Watanabe, K., ... & van den Heuvel, M. P. (2022). Statistical testing in transcriptomic□neuroimaging studies: A how□to and evaluation of methods assessing spatial and gene specificity (Vol. 43, No. 3, pp. 885-901). Hoboken, USA: John Wiley & Sons, Inc..

Weintraub, S., Dikmen, S. S., Heaton, R. K., Tulsky, D. S., Zelazo, P. D., Bauer, P. J., ... & Gershon, R. C. (2013). Cognition assessment using the NIH Toolbox. *Neurology*, 80 (11 Supplement 3), S54-S64.

Weiskopf, N., Edwards, L. J., Helms, G., Mohammadi, S., & Kirilina, E. (2021). Quantitative magnetic resonance imaging of brain anatomy and in vivo histology. *Nature Reviews Physics*, 3(8), 570-588.

Wulff, P., Ponomarenko, A. A., Bartos, M., Korotkova, T. M., Fuchs, E. C., Bähner, F., ... & Monyer, H. (2009). Hippocampal theta rhythm and its coupling with gamma oscillations require fast inhibition onto parvalbumin-positive interneurons. *Proceedings of the National Academy of Sciences*, 106(9), 3561-3566.

Zhao, X., Shi, J., Dai, F., Wei, L., Zhang, B., Yu, X., ... & Wang, H. (2021). Brain development from newborn to adolescence: evaluation by neurite orientation dispersion and density imaging. *Frontiers in Human Neuroscience*, 15, 616132.

Data availability

Raw data is freely available through the Human Connectome Project, upon completion of a data-usage agreement: [https://nda.nih.gov/general-query.html?q=query=featured-datasets:HCP%20Aging%20and%20Development]. Preprocessed data (volumes and microstructures for subfields and anterior/body/posterior subregions) is available in the Supplementary material. Note: volumes are in mm^3, DTI measures (MD, AD, RD) are in units mm^2/s, and IQ is measured via the matrix reasoning subtest.

Figure legends

Fig 1. Subfieds show distinct microstructural profiles
(A) Variance in microstructural measures (NDI, ODI, MD, RD, AD) accounted for by PLS-DA components. (B) The ability of each PLS component to classify subfields, based on the cross-validated accuracy of a support vector classifier (SVC). The total accuracy is based on a classifier trained on all three PLS components (C) Loadings of each microstructural metric onto the first three PLS components (e.g., subfields that score high on PLS1 show high MD and RD), (D) PLS-score plots, showing the distribution of subfields in the space defined by the significant PLS components. The main diagonal includes kernel density estimates of the distribution of each component (e.g., subfields that are mainly distributed to the right in the PLS1 distribution have high scores on PLS1).

Fig 2. Longitudinal-positions show distinct microstructural profiles
(A) Variance in microstructural-measures accounted for by PLS-DA components. (B) The ability of each PLS component to classify longitudinal-positions. (C) Loadings of each microstructural metric onto PLS1. (D) Kernel density estimates of PLS1 scores for each longitudinal-position.

Fig 3. Prominent age/memory-related differences in microstructure across subfields
(A) Bar plot showing how microstructural measures across subfields load onto the latent variable of *X* identified by PLS. Error bars show the boot-strap ratio (BS-Ratio). Significant

features are darkened. (B) Same as A, with loadings of *Y* (the behavioural matrix). (C) The cumulative variance in *X* (microstructural measures) and *Y* (age/memory) accounted for by an increasing number of PLS components. The elbow in this plot demonstrates that the majority of variance which can be accounted for in age by microstructure is captured by PLS1. (D) The covariance between microstructural measures (*X*) and age/memory measures (*Y*) captured by the latent variables.

Fig 4. Prominent age/memory-related differences in microstructure across longitudinal-positions
(A) Bar plot showing how microstructural measures across the longitudinal axis load onto the latent variable of *X* identified by PLS. Error bars show the boot-strap ratio (BS-Ratio). Significant features are darkened. (B) Same as A, with loadings of *Y* (the behavioural matrix). (C) The cumulative variance in *X* and *Y* accounted for by an increasing number of PLS components. (D) Scores (i.e., the projections of *X* and *Y* onto the 1st PLS component), illustrating the covariance between *X* and *Y* captured by the latent variables.

Fig 5. Individual differences in neurite density and orientation dispersion are most sensitive to differences in age
(A) Bar plots showing the coefficient of determination (R^2) for an ordinary least squares regression model predicting age, for each microstructural metric (all ROIs included in model). (B) Same as in A, for a model predicting scores on the NIH picture-sequence memory test. Error bars show the 95% confidence intervals estimated through bootstrap resampling.

Fig 6. Age-related differences in neurite density are observed across subfields and longitudinal-positions
(A) Scatter plots showing the average Neurite Density Index of each subfield with age, along with smoothing splines and bootstrapped standard error. Bar plot shows the variance in age accounted for by each smoothing spline, estimated through cross-validation (out-of-sample R^2) (B) Same as *A*, for longitudinal-positions.

Fig 7. Age-related differences in neurite orientation dispersion are subfield and long-axis specific
(A) Scatter plots showing the average Orientation Dispersion Index of each subfield with age, along with smoothing splines and bootstrapped standard error. Bar plot shows the out-of-sample R^2 for each smoothing spline, estimated through cross-validation (B) Same as *A* for longitudinal position.

Fig 8. Age-related differences in neurite orientation dispersion colocalize with the expression of genes involved in modulating memory-related low-theta oscillations
(A) WM12 genes and their loading onto the 1st PLS component. The majority of genes loaded positively onto the PLS component. Error bars show the boot-strap ratio. (B) Scatterplot showing WM12-gene expression (*X* scores) and age-related change in ODI (*Y* scores) from the PLS component. Each observation is a hippocampal site: at each site, *X*-scores can be calculated by taking the weighted sum of gene-expression values for the genes in panel *A*, *Y*-scores are a normalized measure of age-related change in ODI. (C) False discovery rate (FDR) corrected *p*-values from the cellular component enrichment analyses of the genes which positively load onto the PLS component (D) Same as *C*, for molecular function enrichment analyses.

Fig 9. Distribution of WM12 scores across hippocampal subregions
(A) Boxplots showing the distribution of scores on the WM12 PLS component for each subfield. The weights for this component are a linear combination of gene expressions for the genes in WM12, weighted by the loadings shown in Figure 8A. One-sample *t*-tests assess whether the expression of WM12-genes in each subfield is significantly different from zero. (B) Same as *A*, for anterior/body/posterior subregions.

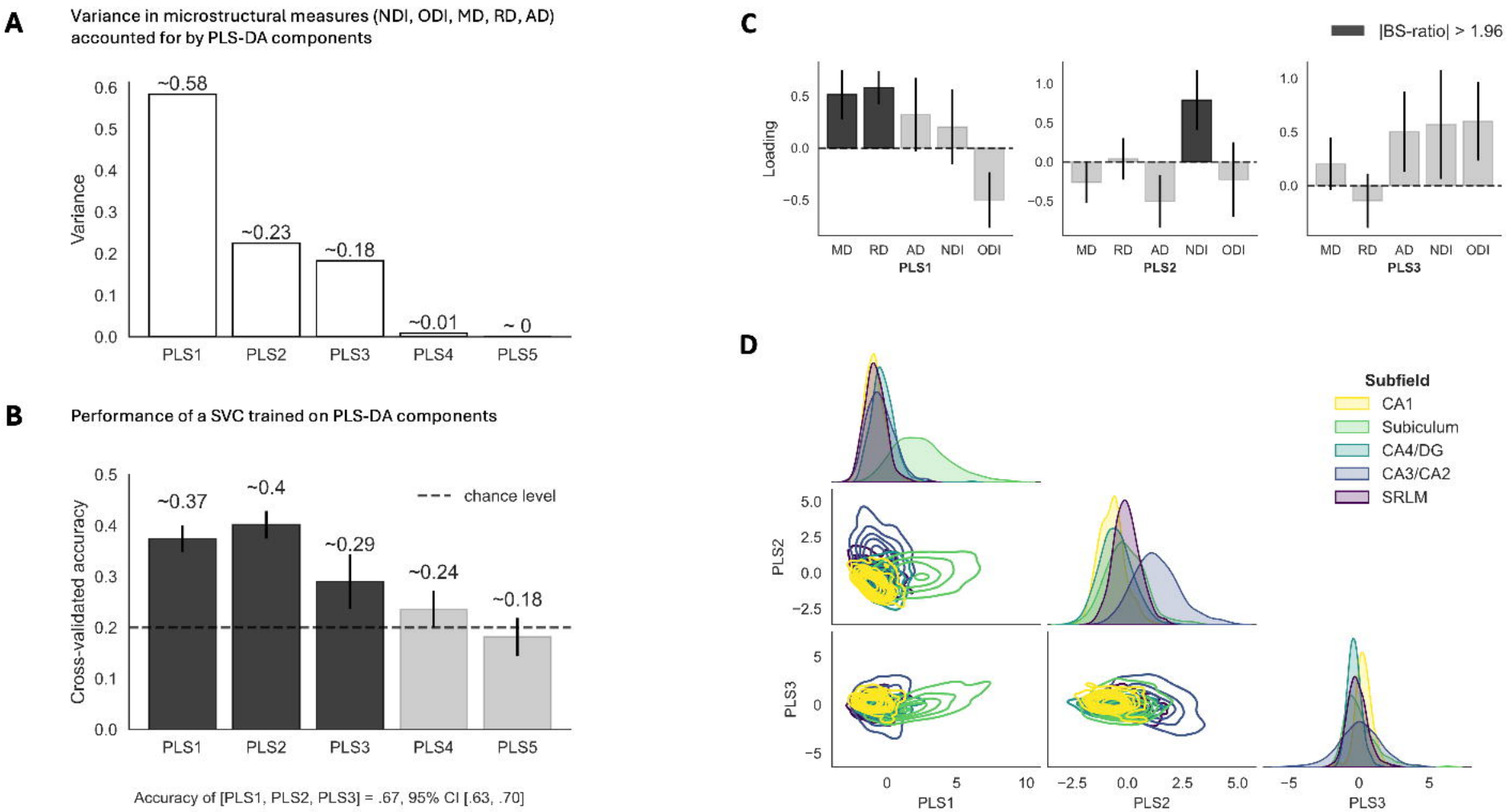
A
Variance in microstructural measures (NDI, ODI, MD, RD, AD) accounted for by PLS-DA components
Variance
~0.58
~0.23
~0.18
~0.01
~ 0
PLS1
PLS2
PLS3
PLS4
PLS5
B
Performance of a SVC trained on PLS-DA components
Cross-validated accuracy
~0.37
~0.4
~0.29
~0.24
~0.18
chance level
Accuracy of [PLS1, PLS2, PLS3] = .67, 95% CI [.63, .70]
C
|BS-ratio| > 1.96
Loading
MD
RD
AD
NDI
ODI
PLS1
PLS2
PLS3
D
Subfield
CA1
Subiculum
CA4/DG
CA3/CA2
SRLM

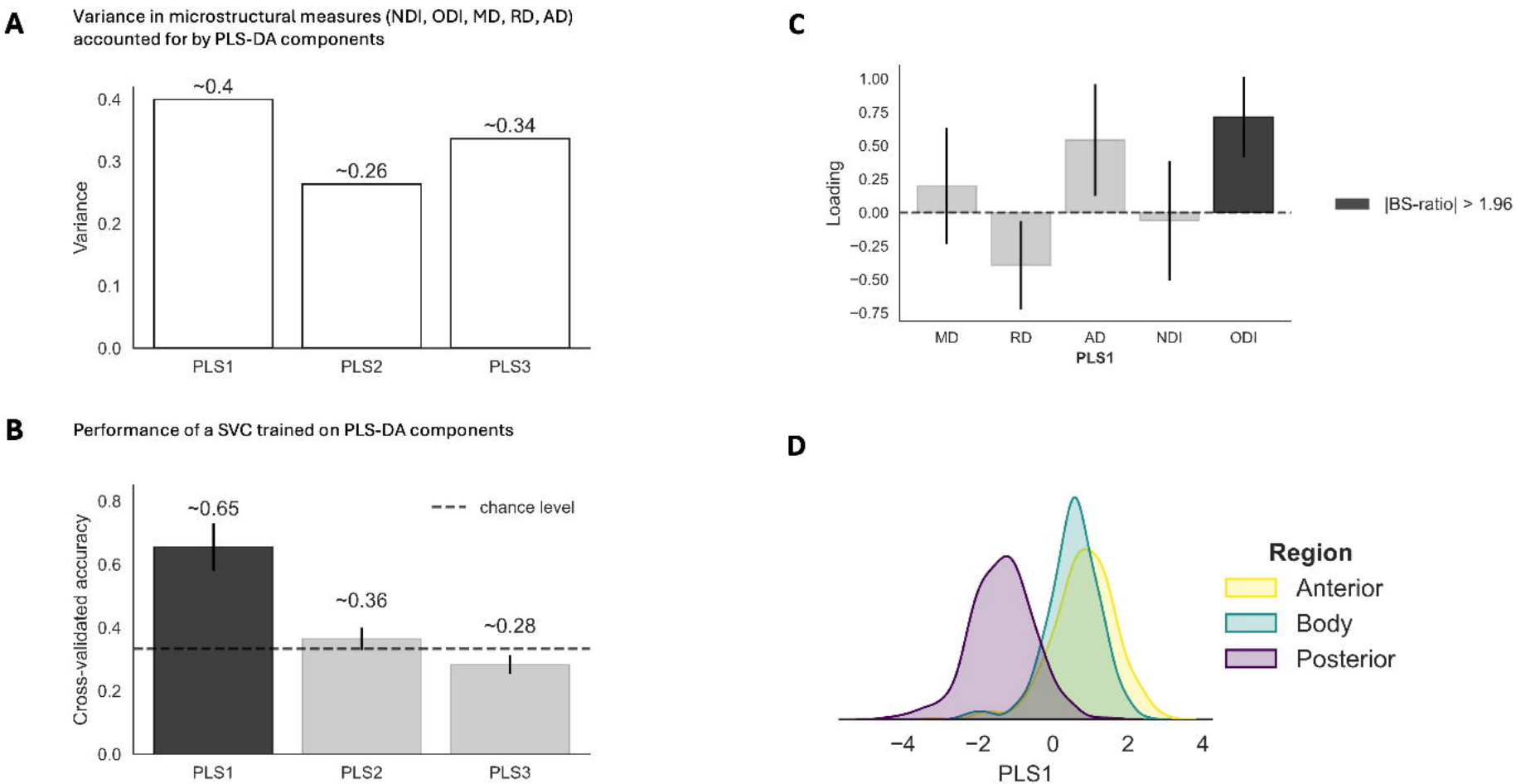
A
Variance in microstructural measures (NDI, ODI, MD, RD, AD) accounted for by PLS-DA components
Variance
0.0
0.1
0.2
0.3
0.4
~0.4
~0.26
~0.34
PLS1
PLS2
PLS3
B
Performance of a SVC trained on PLS-DA components
Cross-validated accuracy
0.0
0.2
0.4
0.6
0.8
~0.65
~0.36
~0.28
chance level
PLS1
PLS2
PLS3
C
Loading
1.00
0.75
0.50
0.25
0.00
−0.25
−0.50
−0.75
MD
RD
AD
NDI
ODI
PLS1
|BS-ratio| > 1.96
D
Region
Anterior
Body
Posterior
−4
−2
0
2
4
PLS1

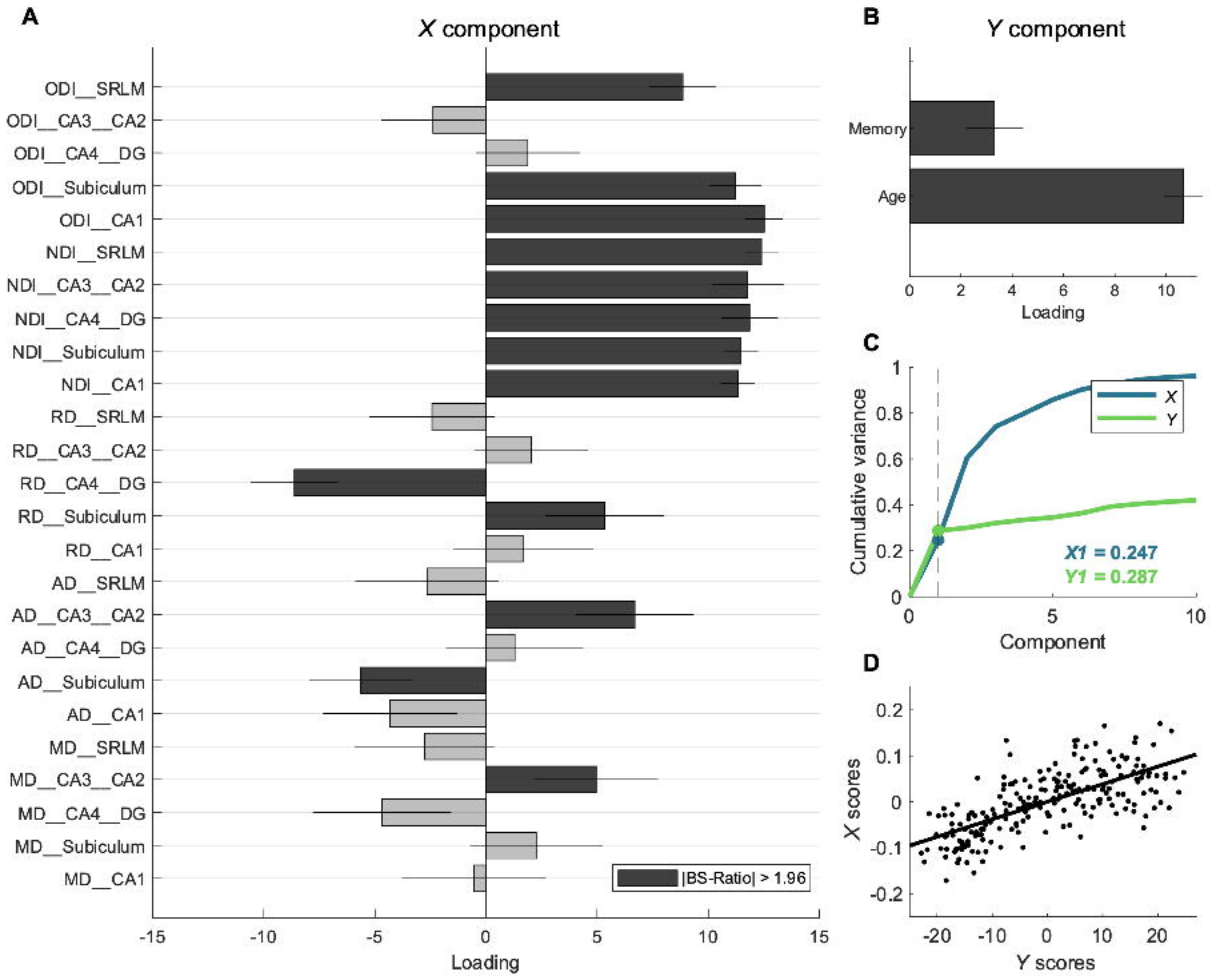
A
X component
ODI__SRLM
ODI__CA3__CA2
ODI__CA4__DG
ODI__Subiculum
ODI__CA1
NDI__SRLM
NDI__CA3__CA2
NDI__CA4__DG
NDI__Subiculum
NDI__CA1
RD__SRLM
RD__CA3__CA2
RD__CA4__DG
RD__Subiculum
RD__CA1
AD__SRLM
AD__CA3__CA2
AD__CA4__DG
AD__Subiculum
AD__CA1
MD__SRLM
MD__CA3__CA2
MD__CA4__DG
MD__Subiculum
MD__CA1
|BS-Ratio| > 1.96
-15
-10
-5
0
5
10
15
Loading
B
Y component
Memory
Age
0
2
4
6
8
10
Loading
C
Cumulative variance
1
0.8
0.6
0.4
0.2
0
X
Y
X1 = 0.247
Y1 = 0.287
0
5
10
Component
D
X scores
0.2
0.1
0
-0.1
-0.2
-20
-10
0
10
20
Y scores

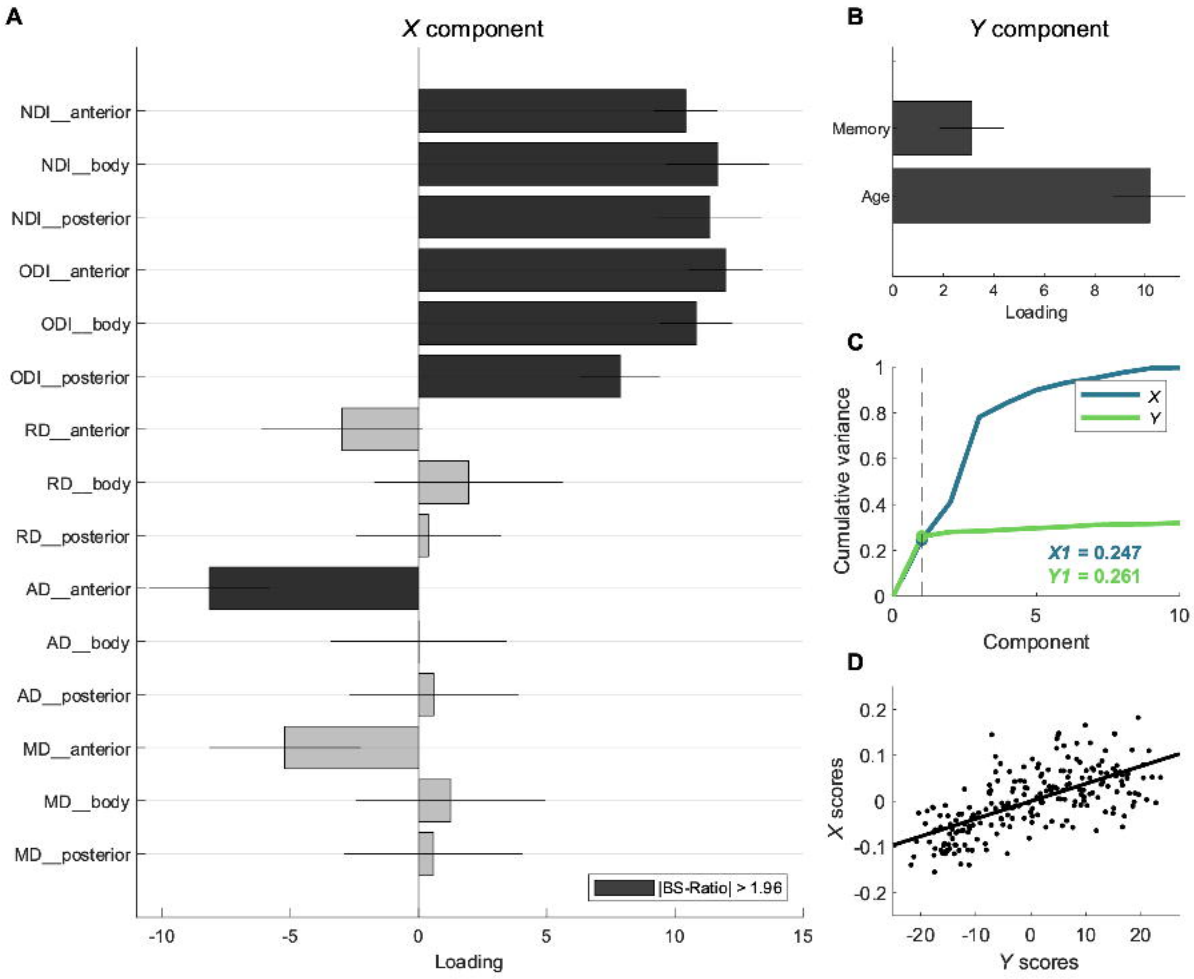
A
X component
NDI__anterior
NDI__body
NDI__posterior
ODI__anterior
ODI__body
ODI__posterior
RD__anterior
RD__body
RD__posterior
AD__anterior
AD__body
AD__posterior
MD__anterior
MD__body
MD__posterior
|BS-Ratio| > 1.96
-10
-5
0
5
10
15
Loading
B
Y component
Memory
Age
0
2
4
6
8
10
Loading
C
Cumulative variance
1
0.8
0.6
0.4
0.2
0
X
Y
X1 = 0.247
Y1 = 0.261
0
5
10
Component
D
X scores
0.2
0.1
0
-0.1
-0.2
-20
-10
0
10
20
Y scores

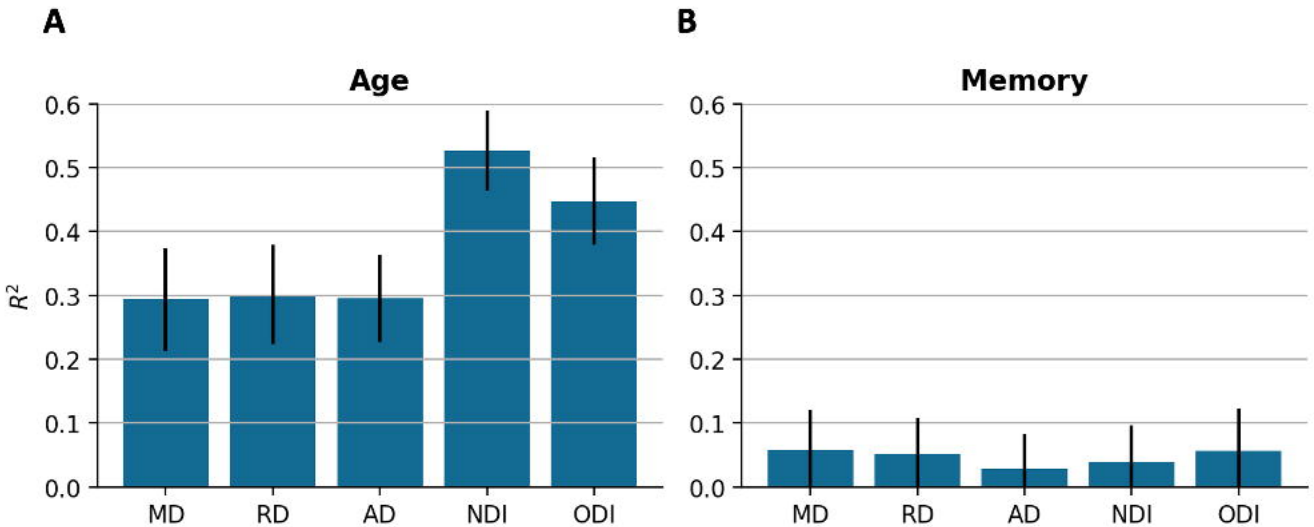
A
Age
B
Memory
R^2
0.0
0.1
0.2
0.3
0.4
0.5
0.6
MD
RD
AD
NDI
ODI

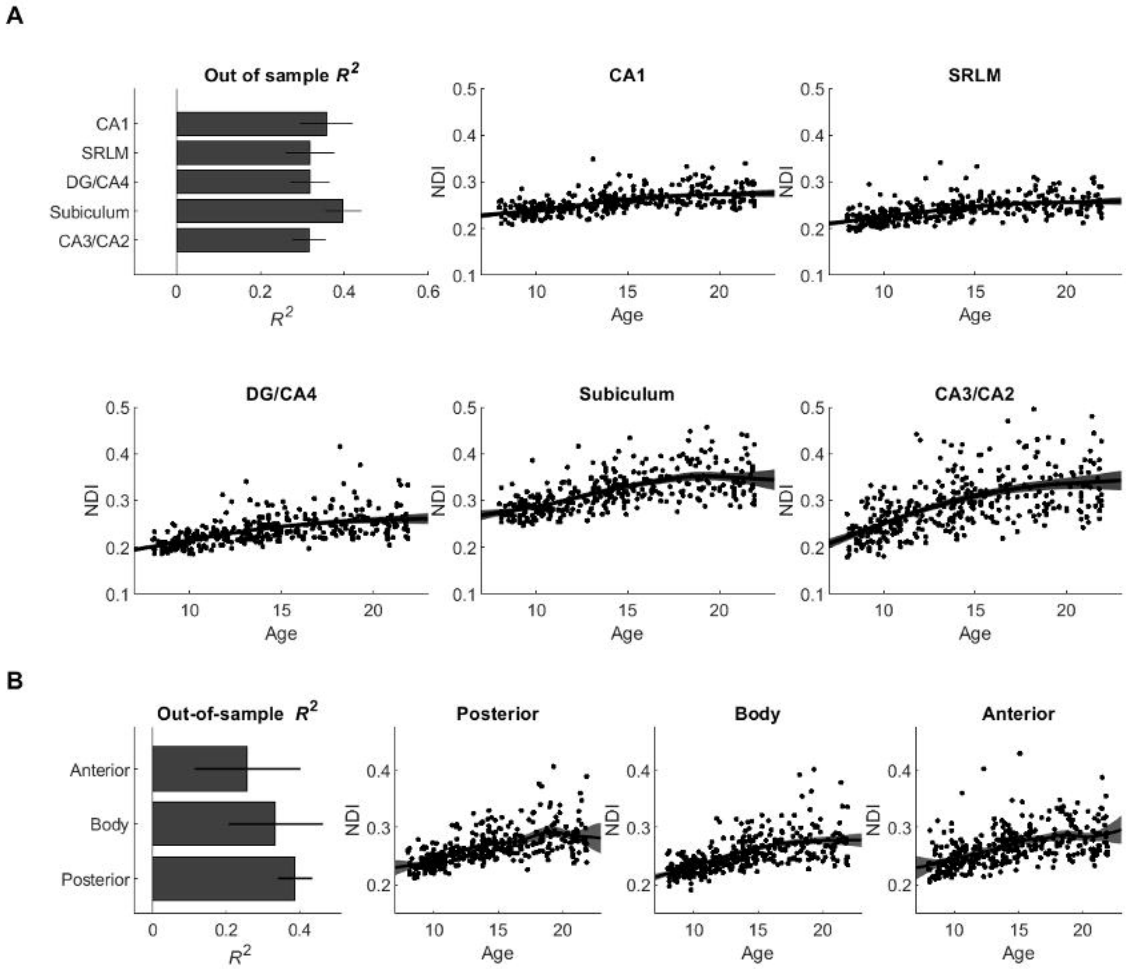
A
Out of sample R^2
CA1
SRLM
DG/CA4
Subiculum
CA3/CA2
0
0.2
0.4
0.6
R^2
CA1
SRLM
DG/CA4
Subiculum
CA3/CA2
NDI
0.1
0.2
0.3
0.4
0.5
10
15
20
Age
B
Out-of-sample R^2
Anterior
Body
Posterior
0
0.2
0.4
R^2
Posterior
Body
Anterior
NDI
0.2
0.3
0.4
10
15
20
Age

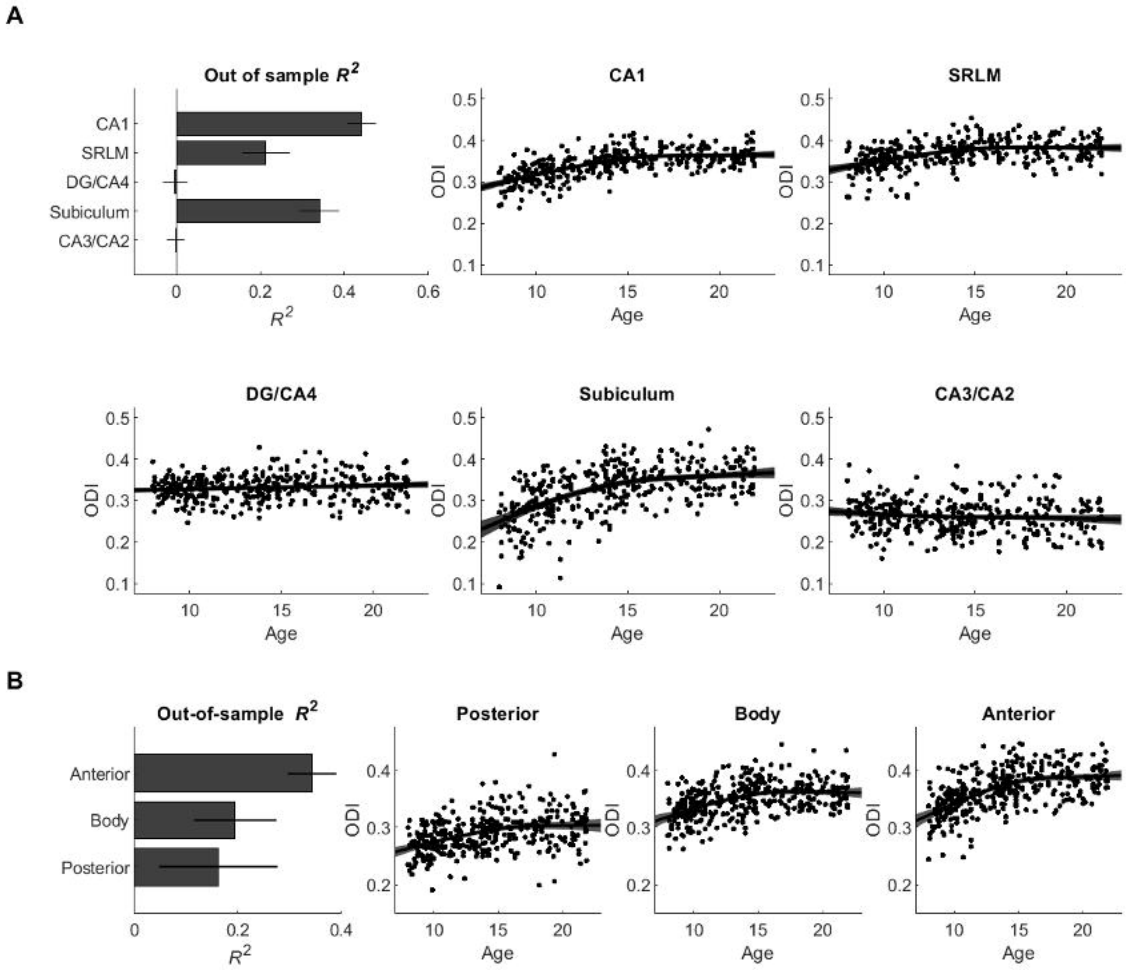
A
Out of sample R^2
CA1
SRLM
DG/CA4
Subiculum
CA3/CA2
0
0.2
0.4
0.6
R^2
CA1
SRLM
DG/CA4
Subiculum
CA3/CA2
ODI
Age
0.1
0.2
0.3
0.4
0.5
10
15
20
B
Out-of-sample R^2
Anterior
Body
Posterior
0
0.2
0.4
R^2
Posterior
Body
Anterior
ODI
Age

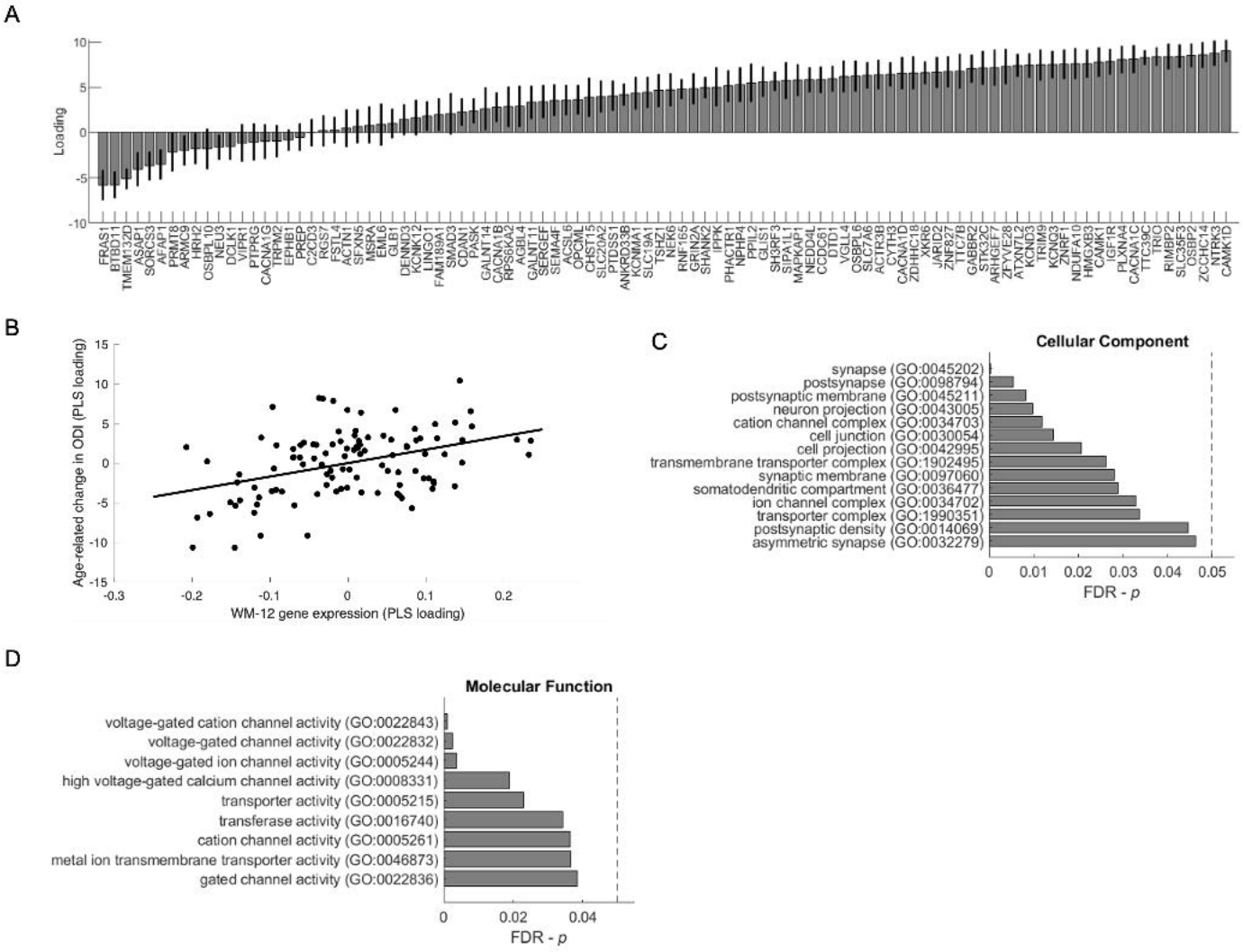
A
Loading
10
5
0
-5
-10
FRAS1 BTBD11 TMEM132D ASAP1 SOX5 ARFIP1 PRMT8 ARMC9 HRH2 OSBPL10 NEU3 DCLK1 VIPR1 PTPRG CACNA1G TRPM2 EPHB1 PREP CZCD3 RGS7 FSTL4 ACTN1 SFXN5 MSRA EML6 GLB1 DENND3 KCNK12 LINGO1 FAM189A1 SMAD3 CDAN1 PASK GALNT14 CACNA1B RPS6KA2 AGBL4 GALNT11 SERGEF SEMA4F ACSL6 CPSF1 CHSTL CPSF1 SLC20A2 PTDSS1 ANKRD33B KCNMA1 SLC19A1 TSHZ1 NEK6 RNF165 GRIN2A SHANK2 ITPK PHACTR3 NPHP4 PPIL2 GLIS1 SH3RF3 SIPA1L1 MAPKAP1 NEDD4L CCDC61 DTD1 VGLL4 OSBPL6 SLC7A6 ACTR3B CYTH3 CACNA1D ZDHHC18 XKR6 JARID2 ZNF827 TTC7B GABBR2 STK32C ARHGEF7 ZNF728 ATXN7 KCND3 TRIM9 KCNQ3 ZNRF1 NDUFA10 HMGXB3 CAMK1 IGF1R PLXNA4 CACNA1C TTC29 TRO RIMBP2 SLC35F3 OSBP2 ZCCHC14 NTRK3 CAMK1D
B
Age-related change in ODI (PLS loading)
15
10
5
0
-5
-10
-15
-0.3
-0.2
-0.1
0
0.1
0.2
WM-12 gene expression (PLS loading)
C
Cellular Component
synapse (GO:0045202)
postsynapse (GO:0098794)
postsynaptic membrane (GO:0045211)
neuron projection (GO:0043005)
cation channel complex (GO:0034703)
cell junction (GO:0030054)
cell projection (GO:0042995)
transmembrane transporter complex (GO:1902495)
synaptic membrane (GO:0097060)
somatodendritic compartment (GO:0036477)
ion channel complex (GO:0034702)
transporter complex (GO:1990351)
postsynaptic density (GO:0014069)
asymmetric synapse (GO:0032279)
0
0.01
0.02
0.03
0.04
0.05
FDR - p
D
Molecular Function
voltage-gated cation channel activity (GO:0022843)
voltage-gated channel activity (GO:0022832)
voltage-gated ion channel activity (GO:0005244)
high voltage-gated calcium channel activity (GO:0008331)
transporter activity (GO:0005215)
transferase activity (GO:0016740)
cation channel activity (GO:0005261)
metal ion transmembrane transporter activity (GO:0046873)
gated channel activity (GO:0022836)
0
0.02
0.04
FDR - p

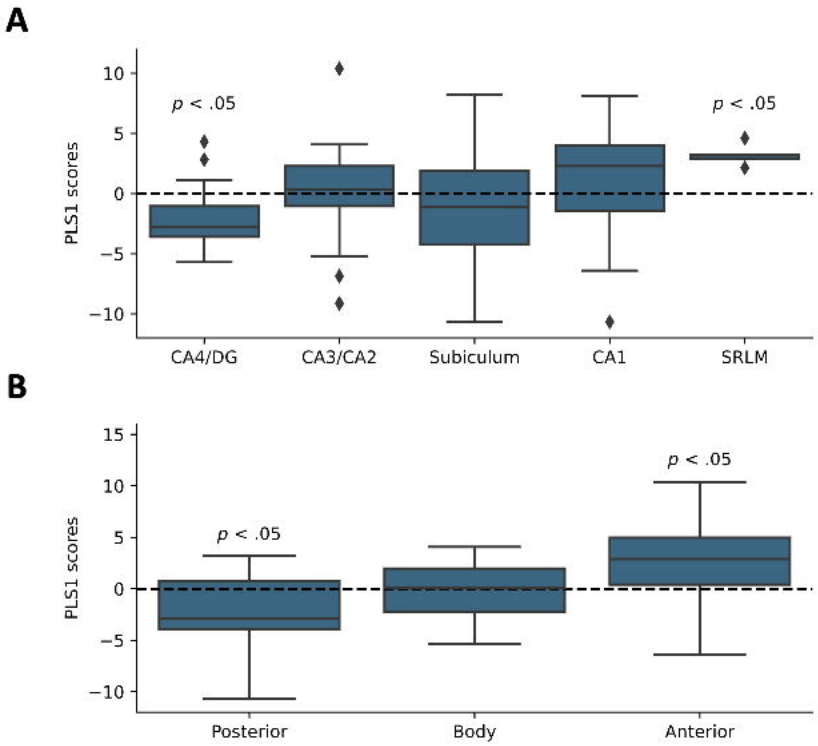
A
10
5
0
−5
−10
PLS1 scores
p < .05
p < .05
CA4/DG
CA3/CA2
Subiculum
CA1
SRLM
B
15
10
5
0
−5
−10
PLS1 scores
p < .05
p < .05
Posterior
Body
Anterior